Hydrodynamic instability of free river bars

Cite as: Phys. Fluids **33**, 045105 (2021); https://doi.org/10.1063/5.0045530
Submitted: 27 January 2021 . Accepted: 10 March 2021 . Published Online: 02 April 2021

Rajesh Kumar Mahato, Sk Zeeshan Ali, and Subhasish Dey

Physics of Fluids ARTICLE scitation.org/journal/phf

Hydrodynamic instability of free river bars

Cite as: Phys. Fluids **33**, 045105 (2021); doi: 10.1063/5.0045530
Submitted: 27 January 2021 · Accepted: 10 March 2021 ·
Published Online: 2 April 2021

Rajesh Kumar Mahato,[1,a] Sk Zeeshan Ali,[2,b] and Subhasish Dey[1,3,c]

AFFILIATIONS

[1]Department of Civil Engineering, Indian Institute of Technology Kharagpur, West Bengal 721302, India
[2]Department of Civil Engineering, Indian Institute of Technology Hyderabad, Telangana 502285, India
[3]Department of Hydraulic Engineering, State Key Laboratory of Hydro-Science and Engineering, Tsinghua University, Beijing 100084, China

[a]rkm22@iitkgp.ac.in
[b]zeeshan@ce.iith.ac.in
[c]Author to whom correspondence should be addressed: sdey@iitkgp.ac.in

ABSTRACT

In this paper, we explore the hydrodynamic instability of free river bars driven by a weakly varying turbulent flow in a straight alluvial channel with erodible bed and non-erodible banks. We employ linear stability analysis in the framework of depth-averaged formulations for the hydrodynamics and the sediment transport. A significant fraction of the sediment flux is considered to be in suspension. The analysis is performed for the alternate pattern of river bars at the leading order followed by the next order, covering the effects of flow regime. We find that the unstable region bounded by a marginal stability curve depends significantly on the shear Reynolds number, which demarcates different flow regimes, and the Shields number and the relative roughness (particle size to flow depth ratio). The results at the next order stabilize the bars with longer wavenumbers. The variations of threshold aspect ratio with Shields number and relative roughness are studied for different flow regimes. In addition, for a given Shields number and relative roughness, the diagram of threshold aspect ratio vs shear Reynolds number is explained. Unlike the conventional theories of bar instability, the analysis reveals limiting values of Shields number and relative roughness beyond which the theoretical results at the next order produce infeasible regions of instability. The limiting values of Shields number and relative roughness appear to reduce, as the shear Reynolds number increases.

I. INTRODUCTION

Riverbed erosion and deposition associated with the interaction between a flowing fluid and an erodible bed form striking sedimentary patterns over widely varying length scales.[1] River bars are frequently observed in both gravel and sand-bed rivers. They are large-scale sedimentary patterns with a wavelength of the order of several channel widths.[2,3] Bars are broadly grouped into two classes: free and forced bars.[1,4] Instability of an erodible bed in a straight channel leads to the formation of free bars.[5] On the other hand, forcing effects (channel curvature and width variation) trigger the formation of forced bars.[1] This study mainly puts into focus the hydrodynamic instability of free bars, as they are the most common depositional features in a straight fluvial system. The formation of river bars limits navigation, increases flood risk, and is linked with scour at banks and bridge piers.[3,6] Moreover, bars play a key role in governing the dynamics of meandering and braided rivers.[1] Therefore, from an engineering perspective, instability of river bars is a key to understanding their precise formation.

Formation of river bars has been studied extensively by means of theoretical analyses,[2,4–12] laboratory experiments,[3,13–17] field observations,[18,19] and numerical simulations.[20,21] Recently, Crosato and Mosselman[22] reported an in-depth review on this topic. Instability of river bars is conventionally analyzed using linear and nonlinear approaches.[1,9,12] A linear stability analysis predicts the unstable region on a plane formed by the channel aspect ratio (channel width to flow depth ratio) and the bar wavenumber. On the other hand, a nonlinear stability analysis quantifies the bar amplitude.

Sediment transport plays a crucial role toward the instability of river bars. Some studies based on two-dimensional (2D) assumptions considered only the bedload flux in the linear stability analysis.[2,9,10] It was found that the channel bed becomes unstable beyond a threshold aspect ratio.[9] Tubino *et al.*[5] studied the instability of free river bars by means of a 3D framework, considering the effects of sediment suspension. They concluded that the inclusion of sediment suspension leads to a decrease in the threshold aspect ratio and an increase in the bar wavelength. Similar findings were reported by Federici and Seminara[11]

and Bertagni and Camporeale.[12] In a slowly varying flow, Federici and Seminara[11] studied the formation of river bars applying the depth-averaged formulations for the hydrodynamics and the sediment transport. Considering only the bedload flux, Federici and Seminara[4] studied the convective nature of bar instability by means of branch point singularities of the dispersion relation. Solving the nonlinear problem numerically, they concluded that groups of bars, emanating from either an arbitrary distributed or a local bed topography perturbation, grow and propagate downstream, keeping the source area intact. Afterward, Federici and Seminara[11] recognized that the inclusion of sediment suspension does not change the nature of bar instability.

The formation of alternate bars was found to be influenced by the flow unsteadiness. Tubino[6] predicted the bar amplitude in an unsteady flow, performing a weakly nonlinear analysis close to the neighborhood of the threshold condition for the bar formation. In addition, Hall[10] presented a linear stability analysis of alternate bars in an unsteady flow. It was found that the flow unsteadiness leads to a reduction in the threshold aspect ratio and the bar wavelength. Lanzoni and Tubino[2] studied the effects of sediment heterogeneity on the formation of alternate bars. They found that the growth rate, wavelength, and propagation speed of bars dampen owing to the presence of sediment heterogeneity.

The state-of-the-art of bar instability is quite mature as far as the flow is steady and the primary mode of sediment transport is the bedload transport. It is well-known that the channel aspect ratio is the key parameter controlling the formation of alternate bars. Earlier studies reported that the sediment suspension plays a destabilizing role by reducing the threshold aspect ratio. This conclusion was drawn with respect to the conventional treatment, where the sediment transport occurs mainly as a bedload transport.[5,11,12] However, this destabilizing influence is yet to be explored in detail. Recently, Ali and Dey[7,8] reported a comprehensive analysis of the instability of large-scale river bars considering the effects of sediment suspension and flow regimes. However, little is so far known about the effects of sediment suspension and flow regime on the bar instability at various orders of approximation.

This study aims at exploring the effects of sediment suspension and flow regime on the bar instability. We perform a linear stability analysis considering a weakly varying turbulent flow in a straight channel with erodible bed and non-erodible banks. For the hydrodynamics and the sediment transport, a depth-averaged formulation is used. The analysis is capable to capture the bar instability over a wide range of shear Reynolds numbers, Shields numbers and relative roughness. It is revealed that the threshold aspect ratio, being the controlling parameter for the bar formation, significantly varies with the shear Reynolds number, Shields number, and relative roughness.

The paper is arranged as follows: The mathematical formulation is presented in Sec. II. The linear stability analysis is performed in Sec. III. The results and discussion are furnished in Sec. IV. Finally, conclusions are drawn in Sec. V.

II. MATHEMATICAL FORMULATION

The schematic of free river bars is shown in Fig. 1. The bar wavelength is represented by λ [Fig. 1(a)]. We consider a 2D turbulent flow of an incompressible fluid in a straight alluvial channel of constant width $2B$. The channel has an erodible bed and non-erodible banks. In Fig. 1(a), x and y represent the streamwise and spanwise directions, respectively. The origin of the coordinate system lies on the channel centerline. Figure 1(b) displays an exemplary cross-sectional view of the channel at a cross section S_1–S_2. In Fig. 1(b), D is the local flow depth and H is the elevation of the free surface of flow from a horizontal reference level. The broken line in Fig. 1(b) characterizes the undisturbed channel cross section.

The depth-averaged momentum and continuity equations can be obtained by performing depth-averaging of the time-averaged momentum and continuity equations, in addition to the appropriate boundary conditions at the free surface and the bed. The time-averaged pressure intensity is assumed to follow the hydrostatic law. As the wavelength of river bars is of the order of a few channel widths, the use of depth-averaged hydrodynamic equations is justified. In addition, the morphological timescale is much larger than the flow timescale. Therefore, we consider the flow field to be a quasi-steady. Let the components of depth-averaged velocity, bed shear stress, bedload flux, and suspended load flux in (x, y) be (U, V), (T_x, T_y), (Q_{bx}, Q_{by}), and (Q_{sx}, Q_{sy}), respectively.

The depth-averaged momentum equations are expressed as[23]

$$\hat{U}\frac{\partial \hat{U}}{\partial \hat{x}} + \hat{V}\frac{\partial \hat{U}}{\partial \hat{y}} + \frac{\partial \hat{H}}{\partial \hat{x}} + \beta\frac{\hat{T}_x}{\hat{D}} = 0, \tag{1}$$

$$\hat{U}\frac{\partial \hat{V}}{\partial \hat{x}} + \hat{V}\frac{\partial \hat{V}}{\partial \hat{y}} + \frac{\partial \hat{H}}{\partial \hat{y}} + \beta\frac{\hat{T}_y}{\hat{D}} = 0. \tag{2}$$

The depth-averaged continuity equation of the fluid phase is expressed as[23]

$$\frac{\partial}{\partial \hat{x}}(\hat{D}\hat{U}) + \frac{\partial}{\partial \hat{y}}(\hat{D}\hat{V}) = 0. \tag{3}$$

The continuity equation of the solid phase, given by Exner,[24] is expressed as

$$\frac{\partial}{\partial \hat{t}}(F^2\hat{H} - \hat{D}) + \gamma\left(\frac{\partial \Phi_{bx}}{\partial \hat{x}} + \frac{\partial \Phi_{by}}{\partial \hat{y}}\right) + \frac{1}{1-p}\left(\frac{\partial \Phi_{sx}}{\partial \hat{x}} + \frac{\partial \Phi_{sy}}{\partial \hat{y}}\right) = 0. \tag{4}$$

In Eqs. (1)–(4), the following dimensionless variables are introduced:

$$\begin{gathered}(\hat{x},\hat{y}) = \frac{(x,y)}{B},\quad \hat{D} = \frac{D}{D_0},\quad \hat{H} = \frac{H}{F^2 D_0},\quad F = \frac{U_0}{(gD_0)^{0.5}},\\ \beta = \frac{B}{D_0},\quad (\hat{U},\hat{V}) = \frac{(U,V)}{U_0},\quad \hat{t} = \frac{tU_0}{B},\quad (\hat{T}_x,\hat{T}_y) = \frac{(T_x,T_y)}{\rho_f U_0^2},\\ (\Phi_{bx},\Phi_{by}) = \frac{(Q_{bx},Q_{by})}{[(s-1)gd^3]^{0.5}},\quad (\Phi_{sx},\Phi_{sy}) = \frac{(Q_{sx},Q_{sy})}{U_0 D_0},\\ \text{and}\quad \gamma = \frac{[(s-1)gd^3]^{0.5}}{(1-p)U_0 D_0},\end{gathered} \tag{5}$$

where F is the undisturbed flow Froude number, U_0 is the undisturbed average flow velocity, g is the gravitational acceleration, β is the channel aspect ratio (channel half-width B to undisturbed flow depth D_0 ratio), t is the time, s is the relative density ($= \rho_s/\rho_f$), ρ_s is the mass density of sediment particles ($= 2650\,\text{kg m}^{-3}$ for natural quartz sand), ρ_f is the mass density of fluid ($= 1000\,\text{kg m}^{-3}$ for water), p is the sediment porosity (≈ 0.3), d is the median sediment size, and γ is the ratio of the scale of sediment flux to that of flow flux.

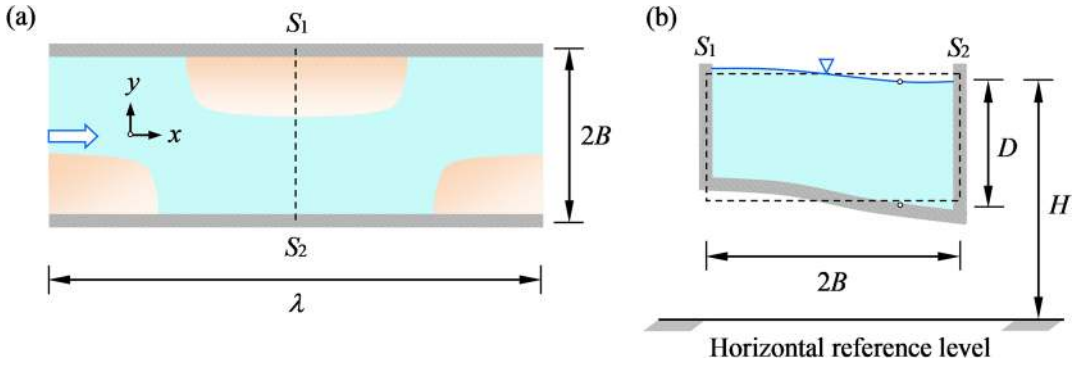

FIG. 1. Definition sketch of the physical system: (a) plan view (flow directed from left to right) and (b) cross-sectional view.

To solve the system of equations, closure relationships for the bed shear stress and the sediment flux vectors are required. The components of the bed shear stress vector, as a function of dynamic pressure, are expressed as

$$(\hat{T}_x, \hat{T}_y) = \frac{f}{8}(\hat{U}, \hat{V})(\hat{U}^2 + \hat{V}^2)^{0.5}, \tag{6}$$

where f is the Darcy–Weisbach friction factor, which describes the resistance due to frictional effects. The f can be determined from the Colebrook–White equation. It is expressed as[25]

$$\frac{1}{f^{0.5}} = -0.86 \ln\left[\frac{2.51}{Rf^{0.5}} + \left(\frac{\hat{k}_s}{14.8\hat{D}}\right)^{1.1}\right], \tag{7}$$

where R is the flow Reynolds number ($= 4UD/\upsilon$), υ is the coefficient of kinematic viscosity of fluid, $\hat{k}_s = k_s/D_0$, and k_s is the bed roughness height. The k_s is expressed as a linear function of particle size, that is, $k_s = \alpha d$, where α is a factor. Following the experimental observations of Engelund and Hansen,[26] we set $\alpha = 2.5$. It is worth mentioning that the Colebrook–White equation facilitates the estimation of friction factor over a wide range of flow regimes. The flow regimes are distinguished by the values of shear Reynolds number R_* as hydraulically smooth ($R_* \leq 3$), transitional ($3 < R_* < 70$), and rough ($R_* \geq 70$) flow regimes. The R_* is expressed as[27]

$$R_* = \frac{u_* k_s}{\upsilon}, \tag{8}$$

where u_* is the shear velocity. The Shields number Θ, representative of the dimensionless fluid-induced bed shear stress, is expressed as[27]

$$\Theta = \frac{u_*^2}{(s-1)gd}. \tag{9}$$

The coupling of R_* with Θ produces

$$R_* = \alpha(\Theta D_*^3)^{0.5}, \tag{10}$$

where D_* is the particle parameter $\{= d[(s-1)g/\upsilon^2]^{1/3}\}$. As the suspended load transport is considered to be dominant in the analysis, the Shields number Θ always exceeds the threshold of sediment suspension Θ_s. It implies that for $\Theta < \Theta_s$, the sediment suspension ceases. For the estimation of Θ_s, we use the empirical formula of van Rijn[28] (see Appendix A). The flow Froude number F and flow Reynolds number R can be expressed as follows:

$$F = \left[\frac{8\Theta(s-1)\hat{d}}{f}\right]^{0.5} \text{and } R = \frac{4\hat{D}R_*}{\alpha\hat{d}}\left(\frac{8}{f}\right)^{0.5}, \tag{11}$$

where $\hat{d}$ is the relative roughness ($= d/D_0$).

The bedload transport is defined as the transport of particles in rolling, sliding, and saltating modes.[27] When the fluid-induced bed shear stress just exceeds its threshold value, the particles are transported in sliding and/or rolling mode. With an increase in bed shear stress, the bedload transport occurs in a saltating mode.[27,29] As the bed shear stress increases further, finer particles are lifted up into suspension owing to the upward diffusion of near-bed turbulence.[27] In this situation, both the bedload and suspended load transport exist. The direction of bedload transport deviates from that of bed shear stress.[30–32] The components of bedload flux vector are expressed as

$$(\Phi_{bx}, \Phi_{by}) = \Phi(\cos\chi, \sin\chi), \tag{12}$$

where Φ is the bedload flux intensity and χ is the angle between the resultant bedload flux and the longitudinal direction. The χ can be obtained by imposing a dynamic equilibrium on a spherical particle moving along a plane tangential to the bed. The χ is expressed as[30]

$$\sin\chi = \frac{\hat{V}}{(\hat{U}^2 + \hat{V}^2)^{0.5}} - \frac{r}{\beta\Theta^{0.5}} \cdot \frac{\partial}{\partial\hat{y}}(F^2\hat{H} - \hat{D}), \tag{13}$$

where r is an empirical constant. The r varies over a certain range, as reported in the literature.[33] However, following the study of Talmon *et al.*,[34] we consider $r = 0.56$ in this study. For the bedload flux intensity Φ, various power laws are available in the literature. Here, we employ the empirical formula of Meyer-Peter and Müller.[35] It is

$$\Phi = 8(\Theta - \Theta_c)^{1.5}, \tag{14}$$

where Θ_c is the threshold Shields number. Note that Ali and Dey[36] obtained the above empirical exponent from the phenomenological theory of turbulence. For the estimation of Θ_c, the force system acting on a particle needs to be analyzed. Interested readers may refer to the work of Ali and Dey[37,38] and Dey and Ali[39–41] in this regard. However,

to simplify the analysis in the present context, we use the following empirical relationship of $\Theta_c(D_*)$, given by Wu and Wang:[42]

$$\Theta_c = KD_*^n. \tag{15}$$

In Eq. (15), the complete set $(K, n) = (0.126, -0.44)$ for $D_* < 1.5$, $(0.131, -0.55)$ for $1.5 \le D_* < 10$, $(0.0685, -0.27)$ for $10 \le D_* < 20$, $(0.0173, 0.19)$ for $20 \le D_* < 40$, $(0.0115, 0.3)$ for $40 \le D_* < 150$, and $(0.052, 0)$ for $D_* \ge 150$.

Following the work of Federici and Seminara[11] and Bertagni and Camporeale,[12] we consider a 2D extension of the depth-averaged model of Bolla Pittaluga and Seminara[43] for the estimation of suspended load flux vector. Considering a slowly varying flow, Bolla Pittaluga and Seminara[43] performed an asymptotic expansion of the exact solution of the advection-diffusion equation of sediment concentration. In the perturbation approach, the effects of advective-cum-unsteadiness are considered to be smaller than those of gravitational settling and turbulent diffusion. Mathematically, it is expressed as

$$\delta_k = \frac{U_0 D_0}{W_s \lambda} \ll 1, \tag{16}$$

where W_s is the settling velocity of particles (see Appendix A) and λ is the scale of longitudinal variation of the flow field ($\approx$ bar wavelength). As the δ_k depends on the bar wavelength, another small parameter δ can be defined as[11,12]

$$\delta = \delta_k \frac{\lambda}{B} = \frac{U_0}{\beta W_s}. \tag{17}$$

The suspended load flux vector can be expressed as[43]

$$(\Phi_{sx}, \Phi_{sy}) = \hat{D}(\hat{U}, \hat{V})\psi, \tag{18}$$

where ψ is a function that can be expended in powers of δ as follows:

$$\psi = \psi_0 + \delta\psi_1 + \mathrm{O}(\delta^2). \tag{19}$$

In the above, ψ_0 is the function for the uniform flow condition and ψ_1 describes the $\mathrm{O}(\delta)$ correction to the function ψ. The correction at $\mathrm{O}(\delta)$ considers weak nonequilibrium effects owing to the spatial variation of the flow field. The functions ψ_0 and ψ_1 are expressed as[43]

$$\psi_0 = C_0 K_0,\ \psi_1 = K_1 \hat{D}\left(\hat{U}\frac{\partial C_0}{\partial \hat{x}} + \hat{V}\frac{\partial C_0}{\partial \hat{y}}\right), \tag{20}$$

where C_0 is the depth-averaged concentration at the leading order, and K_0 and K_1 are the functions of relevant physical parameters (see Appendix B).

Finally, the channel banks are considered to be impervious to the flow and sediment fluxes. Hence, we write

$$\hat{V}|_{\hat{y}=\pm 1} = \Phi_{by}|_{\hat{y}=\pm 1} = \Phi_{sy}|_{\hat{y}=\pm 1} = 0. \tag{21}$$

III. LINEAR STABILITY ANALYSIS

In the linear stability analysis, the primitive variables are expanded as follows:

$$(\hat{U}, \hat{V}, \hat{H}, \hat{D}) = (1, 0, \hat{H}_0, 1) + \varepsilon(\hat{U}_1, \hat{V}_1, \hat{H}_1, \hat{D}_1), \tag{22}$$

where ε is a small parameter. The perturbations need to be further expanded in powers of δ in order to account for the weak nonequilibrium effects originating from the spatial variation of the flow field. Therefore, we write

$$(\hat{U}_1, \hat{V}_1, \hat{H}_1, \hat{D}_1) = (\hat{U}_{10}, \hat{V}_{10}, \hat{H}_{10}, \hat{D}_{10}) + \delta(\hat{U}_{11}, \hat{V}_{11}, \hat{H}_{11}, \hat{D}_{11}) + \mathrm{O}(\delta^2). \tag{23}$$

The components of bed shear stress and bedload flux vectors are expressed as

$$\hat{T}_{x10} + \delta\hat{T}_{x11} = \frac{f_0}{8}\left[s_1(\hat{U}_{10} + \delta\hat{U}_{11}) + s_2(\hat{D}_{10} + \delta\hat{D}_{11})\right], \tag{24}$$

$$\hat{T}_{y10} + \delta\hat{T}_{y11} = \frac{f_0}{8}(\hat{V}_{10} + \delta\hat{V}_{11}), \tag{25}$$

$$\Phi_{bx10} + \delta\Phi_{bx11} = \Phi_0\left[s_3(\hat{U}_{10} + \delta\hat{U}_{11}) + s_4(\hat{D}_{10} + \delta\hat{D}_{11})\right], \tag{26}$$

$$\Phi_{by10} + \delta\Phi_{by11} = \Phi_0\left\{(\hat{V}_{10} + \delta\hat{V}_{11}) - \frac{r}{\beta\Theta_0^{0.5}}\cdot\frac{\partial}{\partial\hat{y}} \times\left[F^2(\hat{H}_{10} + \delta\hat{H}_{11}) - (\hat{D}_{10} + \delta\hat{D}_{11})\right]\right\}, \tag{27}$$

where f_0, Φ_0, and Θ_0 are the Darcy–Weisbach friction factor, bedload function, and Shields number, respectively, corresponding to the undisturbed state. The coefficients s_i ($i = 1$ to 4) are given in Appendix C. To perturb the suspended load flux, the ψ_0 and ψ_1 are expanded as follows:

$$\psi_0 = \psi_{00}\{1 + \varepsilon[\psi_{010} + \delta\psi_{011} + \mathrm{O}(\delta^2)]\}, \tag{28}$$

$$\psi_1 = \varepsilon\psi_{110} + \mathrm{O}(\varepsilon\delta), \tag{29}$$

where ψ_{00} is the function ψ_0 at the undisturbed state. The quantities ψ_{010}, ψ_{011}, and ψ_{110} are given in Appendix C.

Substituting Eqs. (22)–(29) into Eqs. (1)–(4), we obtain the following linear differential problem at the leading order $\mathrm{O}(\varepsilon)$:

$$\frac{\partial\hat{U}_{10}}{\partial\hat{x}} + \frac{\partial\hat{H}_{10}}{\partial\hat{x}} + \frac{\beta f_0}{8}\left[s_1\hat{U}_{10} + (s_2 - 1)\hat{D}_{10}\right] = 0, \tag{30}$$

$$\frac{\partial\hat{V}_{10}}{\partial\hat{x}} + \frac{\partial\hat{H}_{10}}{\partial\hat{y}} + \frac{\beta f_0}{8}\hat{V}_{10} = 0, \tag{31}$$

$$\frac{\partial\hat{U}_{10}}{\partial\hat{x}} + \frac{\partial\hat{V}_{10}}{\partial\hat{y}} + \frac{\partial\hat{D}_{10}}{\partial\hat{x}} = 0, \tag{32}$$

$$\frac{\partial}{\partial\hat{t}}(F^2\hat{H}_{10} - \hat{D}_{10}) + \gamma\Phi_0\left[s_3\frac{\partial\hat{U}_{10}}{\partial\hat{x}} + s_4\frac{\partial\hat{D}_{10}}{\partial\hat{x}} + \frac{\partial\hat{V}_{10}}{\partial\hat{y}} - \frac{r}{\beta\Theta_0^{0.5}}\cdot\frac{\partial^2}{\partial\hat{y}^2}(F^2\hat{H}_{10} - \hat{D}_{10})\right] + \frac{\psi_{00}}{1-p}\left(\frac{\partial\hat{U}_{10}}{\partial\hat{x}} + \frac{\partial\hat{D}_{10}}{\partial\hat{x}} + \frac{\partial\hat{V}_{10}}{\partial\hat{y}} + \frac{\partial\psi_{010}}{\partial\hat{x}}\right) = 0. \tag{33}$$

Similarly, the linear differential problem at the next order $\mathrm{O}(\varepsilon\delta)$ is expressed as

$$\frac{\partial\hat{U}_{11}}{\partial\hat{x}} + \frac{\partial\hat{H}_{11}}{\partial\hat{x}} + \frac{\beta f_0}{8}\left[s_1\hat{U}_{11} + (s_2 - 1)\hat{D}_{11}\right] = 0, \tag{34}$$

$$\frac{\partial\hat{V}_{11}}{\partial\hat{x}} + \frac{\partial\hat{H}_{11}}{\partial\hat{y}} + \frac{\beta f_0}{8}\hat{V}_{11} = 0, \tag{35}$$

$$\frac{\partial\hat{U}_{11}}{\partial\hat{x}} + \frac{\partial\hat{V}_{11}}{\partial\hat{y}} + \frac{\partial\hat{D}_{11}}{\partial\hat{x}} = 0, \tag{36}$$

$$\frac{\partial}{\partial \hat{t}}(F^2\hat{H}_{11}-\hat{D}_{11})+\gamma\Phi_0\left[s_3\frac{\partial \hat{U}_{11}}{\partial \hat{x}}+s_4\frac{\partial \hat{D}_{11}}{\partial \hat{x}}+\frac{\partial \hat{V}_{11}}{\partial \hat{y}}-\frac{r}{\beta\Theta_0^{0.5}}\cdot\frac{\partial^2}{\partial \hat{y}^2}(F^2\hat{H}_{11}-\hat{D}_{11})\right]+\frac{1}{1-p}\left[\psi_{00}\left(\frac{\partial \hat{U}_{11}}{\partial \hat{x}}+\frac{\partial \hat{D}_{11}}{\partial \hat{x}}+\frac{\partial \hat{V}_{11}}{\partial \hat{y}}+\frac{\partial \psi_{011}}{\partial \hat{x}}\right)+\frac{\partial \psi_{110}}{\partial \hat{x}}\right]=0. \tag{37}$$

The solution of the problem is sought in the form of normal modes. Therefore, we write

$$(\hat{U}_{1j},\hat{V}_{1j},\hat{H}_{1j},\hat{D}_{1j})|_{m=\text{odd}}=[u_{1j}S_m(\hat{y}),v_{1j}C_m(\hat{y}),h_{1j}S_m(\hat{y}),d_{1j}S_m(\hat{y})]\times\exp\left[\mathrm{i}(\hat{k}\hat{x}-\omega\hat{t})\right]+\text{c.c.}, \tag{38}$$

$$(\hat{U}_{1j},\hat{V}_{1j},\hat{H}_{1j},\hat{D}_{1j})|_{m=\text{even}}=[u_{1j}C_m(\hat{y}),v_{1j}S_m(\hat{y}),h_{1j}C_m(\hat{y}),d_{1j}C_m(\hat{y})]\exp\left[\mathrm{i}(\hat{k}\hat{x}-\omega\hat{t})\right]+\text{c.c.}, \tag{39}$$

where m is the transverse Fourier mode, j is either 0 or 1 depending on the order of approximation, i is the imaginary unit [$=(-1)^{0.5}$], $\hat{k}$ is the dimensionless wavenumber ($=2\pi B/\lambda$), ω is a complex quantity, whose real and imaginary parts represent the growth rate and the dimensionless frequency of perturbations, respectively, when multiplied with –i, and c.c. stands for the complex conjugate. The S_m and C_m are expressed as

$$S_m(\hat{y})=\sin\left(\frac{\pi}{2}m\hat{y}\right), \tag{40}$$

$$C_m(\hat{y})=\cos\left(\frac{\pi}{2}m\hat{y}\right). \tag{41}$$

The complex quantity ω is expanded in powers of δ as

$$\omega=\omega_0+\delta\omega_1+\mathrm{O}(\delta^2), \tag{42}$$

where ω_0 is the value of ω at the leading order and ω_1 is the O(δ) correction to the ω.

When Eqs. (38)–(42) are substituted into the linear differential problem at O(ε), a linear algebraic homogeneous system is obtained. In matrix form, this can be expressed as

$$\mathbf{AU}=0, \tag{43}$$

where $\mathbf{A}=a_{ij}\in\mathbb{R}^{4\times4}$ and $\mathbf{U}=(u_{10},v_{10},h_{10},d_{10})^{\mathrm{T}}$. The matrix coefficients a_{ij} are as follows:

$$\begin{aligned}
a_{11}&=\mathrm{i}\hat{k}+\frac{\beta f_0}{8}s_1,\quad a_{12}=a_{21}=a_{24}=a_{33}=0,\\
a_{13}&=a_{31}=a_{34}=\mathrm{i}\hat{k},\quad a_{14}=\frac{\beta f_0}{8}(s_2-1),\\
a_{22}&=\mathrm{i}\hat{k}+\frac{\beta f_0}{8},\quad a_{23}=(-1)^{1+m}\frac{\pi m}{2},\quad a_{32}=(-1)^m\frac{\pi m}{2},\\
a_{41}&=\left[\gamma\Phi_0 s_3+\frac{\psi_{00}}{1-p}(1+t_1)\right]\mathrm{i}\hat{k},\\
a_{42}&=(-1)^m\frac{\pi m}{2}\left(\gamma\Phi_0+\frac{\psi_{00}}{1-p}\right),\\
a_{43}&=F^2\left[-\mathrm{i}\omega_0+\frac{\gamma r\Phi_0}{\beta\Theta_0^{0.5}}\left(\frac{\pi m}{2}\right)^2\right],\\
a_{44}&=\mathrm{i}\omega_0+\mathrm{i}\hat{k}\gamma\Phi_0 s_4-\frac{\gamma r\Phi_0}{\beta\Theta_0^{0.5}}\left(\frac{\pi m}{2}\right)^2+\mathrm{i}\hat{k}(1+t_2)\frac{\psi_{00}}{1-p}.
\end{aligned} \tag{44}$$

In the above equation, t_1 and t_2 are given in Appendix C.

At O($\varepsilon\delta$), a linear algebraic nonhomogeneous system is obtained as

$$\mathbf{AV}=\mathbf{C}, \tag{45}$$

where $\mathbf{V}=(u_{11},v_{11},h_{11},d_{11})^{\mathrm{T}}$, $\mathbf{C}=(0,0,0,c_{41})^{\mathrm{T}}$, $c_{41}=\mathrm{i}\omega_1(F^2h_{10}-d_{10})+\hat{k}^2(g_1u_{10}+g_2d_{10})$, and g_1 and g_2 are given in Appendix C.

At O(ε), a dispersion relationship emerging from the solvability of Eq. (43) takes the form of

$$\begin{aligned}
-\mathrm{i}\omega_0&\left[F^2(a_{11}a_{34}-a_{14}a_{31})-\left(a_{13}a_{31}+\frac{a_{11}a_{23}a_{32}}{a_{22}}\right)\right]\\
&=\frac{a_{41}}{a_{11}}\left[a_{13}(a_{11}a_{34}-a_{14}a_{31})+a_{14}\left(a_{13}a_{31}+\frac{a_{11}a_{23}a_{32}}{a_{22}}\right)\right]\\
&\quad+(a_{11}a_{34}-a_{14}a_{31})\left(\frac{a_{23}a_{42}}{a_{22}}-\frac{F^2\gamma r\Phi_0\pi^2m^2}{4\beta\Theta_0^{0.5}}\right)\\
&\quad-\left(a_{13}a_{31}+\frac{a_{11}a_{23}a_{32}}{a_{22}}\right)\left[\mathrm{i}\hat{k}\gamma\Phi_0 s_4-\frac{\gamma r\Phi_0\pi^2m^2}{4\beta\Theta_0^{0.5}}\right.\\
&\quad\left.+\mathrm{i}\hat{k}(1+t_2)\frac{\psi_{00}}{1-p}\right].
\end{aligned} \tag{46}$$

We use Eq. (45) to evaluate ω_1. As the homogeneous part of Eq. (45) admits a nontrivial solution, a solvability condition is required. The solvability condition suggests that det($\mathbf{A}$) = 0 after replacing the last column of $\mathbf{A}$ by the column matrix $\mathbf{C}$.[9] Imposition of the solvability condition on Eq. (45) yields

$$\begin{aligned}
-\mathrm{i}\omega_1&\left[F^2(a_{11}a_{34}-a_{14}a_{31})-\left(a_{13}a_{31}+\frac{a_{11}a_{23}a_{32}}{a_{22}}\right)\right]\\
&=\hat{k}^2\left\{g_2\left(a_{13}a_{31}+\frac{a_{11}a_{23}a_{32}}{a_{22}}\right)-\frac{g_1}{a_{11}}\left[a_{13}(a_{11}a_{34}-a_{14}a_{31})\right.\right.\\
&\quad\left.\left.+a_{14}\left(a_{13}a_{31}+\frac{a_{11}a_{23}a_{32}}{a_{22}}\right)\right]\right\}.
\end{aligned} \tag{47}$$

It is worth mentioning that by substituting ω_1 into Eq. (42), the marginal stability (MS) curve correct to O($\varepsilon\delta$) can be obtained. The MS curves at O(ε) and O($\varepsilon\delta$) are defined as Re(–iω_0) = 0 and Re(–iω) = 0, respectively, where Re represents the real part of the complex function.

IV. RESULTS AND DISCUSSION

In this section, computational results are presented for the alternate pattern of river bars ($m=1$). In order to cover various flow regimes, for instance, smooth ($R_*\leq3$), transitional ($3<R_*<70$), and rough ($R_*\geq70$) flow regimes, we consider $R_*=1$ in a smooth flow, $R_*=3$ at the extremity of a smooth flow, $R_*=12$ and 30 (two characteristic values) in transitional flows, and $R_*=100$ in a rough flow. It might appear to the readers that the resolution of the shear Reynolds number selection is limited, as only five characteristic values are considered, and therefore the corresponding simulation results may not capture the entire hydrodynamic instability. However, this is not the case. It may be emphasized here that the selected shear Reynolds numbers correspond to a specific flow regime and therefore, they offer an idea of how the stability pattern evolves with an increase in shear Reynolds number. In the subsequent discussion, it is shown that the

above-mentioned consideration of shear Reynolds numbers is justified in order to identify the stability pattern for an intermediate shear Reynolds number. The MS curves, for a given shear Reynolds number R_*, are presented on the $\beta(\hat{k})$ plane for different values of Shields number Θ and relative roughness $\hat{d}$ (Figs. 2–5). A large value of Θ signifies a considerable amount of sediment suspension, whereas a large value of $\hat{d}$ for a given particle size suggests a shallow flow depth. A typical MS curve demarcates the stable (exterior of the curve) and the unstable (interior of the curve) regions. In a stable (unstable) region, the perturbations decay (amplify) with time.

The MS curves corresponding to a smooth flow regime ($R_* = 1$) are furnished in Fig. 2 on a semi-logarithmic scale. The solid and the dashed lines represent the MS curves at O(ε) and O($\varepsilon\delta$), respectively (also in succeeding Figs. 3–5). At O(ε), the MS curves (solid lines) on the $\beta(\hat{k})$ plane appear to be U-shaped, embracing the region of instability. For a given triplet (R_*, Θ, $\hat{d}$), there exists a single MS curve with local minima ($\hat{k}_c$, β_c), which correspond to $d\beta/d\hat{k} = 0$. This suggests that for $\beta < \beta_c$, the formation of alternate bars is inhibited. Beyond the threshold aspect ratio β_c, the alternate bars are formed over a wide range of wavenumbers.

Figure 2(a) shows the MS curves for a given relative roughness $\hat{d}$ and different Shields numbers Θ. As the shear Reynolds number is kept constant, an increase in Shields number corresponds to a decrease in particle size [Fig. 2(a)]. This is because the particle parameter follows an inverse scaling with the Shields number as $D_* \propto \Theta^{-1/3}$, in accord with Eq. (10).

At O(ε), the unstable region bounded by an MS curve tends to reduce, as the Shields number increases [Fig. 2(a)]. It is attributed to the presence of considerable sediment suspension that imparts a stabilizing effect. The stabilizing effect is more encouraging for a longer wavenumber. This reveals that even for the same aspect ratio, a small Shields number (large particle size) may favor the formation of alternate bars with longer wavenumbers, while a large Shields number (small particle size) may not favor. Similar conclusion can be drawn for the MS curves at O($\varepsilon\delta$) [see dashed lines in Fig. 2(a)]. However, it appears that for a given triplet (R_*, Θ, $\hat{d}$), the MS curve at O($\varepsilon\delta$) holds a smaller unstable region than that at O(ε). Therefore, the longer wavenumbers at O($\varepsilon\delta$) become more stable than those at O(ε). This leads to an enhanced stable region, an observation being in conformity with Federici and Seminara.[11] Note that for shorter wavenumbers ($\hat{k} < 0.04$), the MS curves at O(ε) almost coincide with those at O($\varepsilon\delta$). In Fig. 2(a), the maximum Shields number is taken as 0.62. It has been found that for $\Theta > 0.62$, the MS curve at O($\varepsilon\delta$) produces an infeasible region of instability, which contradicts the classical results. Therefore, $\Theta_m = 0.62$ represents the limiting Shields number for the formation of alternate bars in a smooth flow regime. Notably, this subtle conclusion was not drawn in the previous studies.

It is interesting to find how the threshold aspect ratio β_c varies with the Shields number Θ. To this end, the $\beta_c(\Theta)$ curves at O(ε) and O($\varepsilon\delta$) are plotted in the inset of Fig. 2(a). The $\beta_c(\Theta)$ curves at both orders show similar trend. For a given order, the threshold aspect ratio increases with an increase in Shields number attaining a peak and then reduces, as the Shields number increases further. In addition, for a given Shields number, the threshold aspect ratio at O($\varepsilon\delta$) is larger than that at O(ε). Moreover, the peak of $\beta_c(\Theta)$ curve at O(ε) appears early than that at O($\varepsilon\delta$).

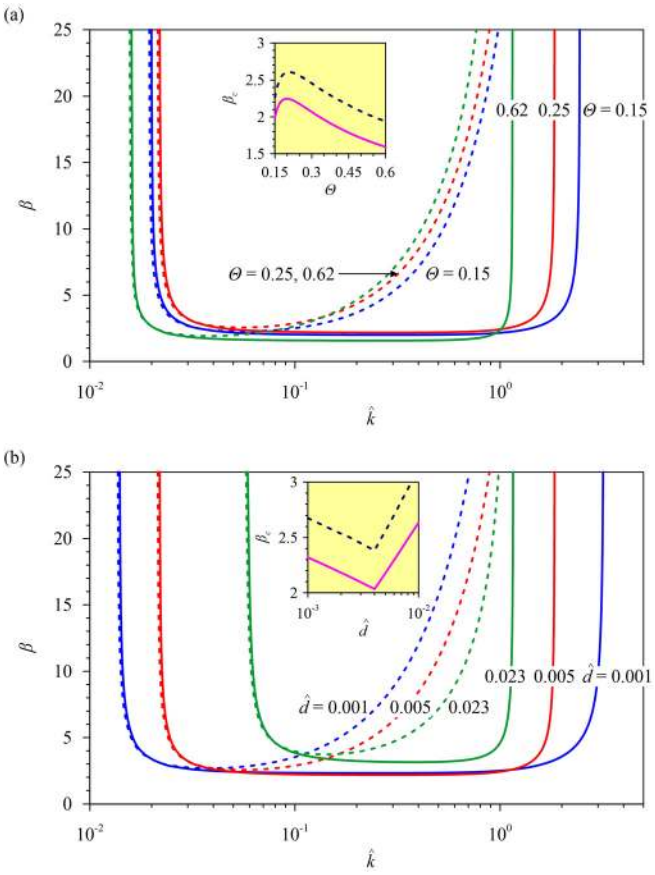

FIG. 2. The MS curves in a smooth flow regime, $R_* = 1$ [solid lines: O(ε) and dashed lines: O($\varepsilon\delta$)]: (a) $\hat{d} = 0.005$ and different values of $\Theta = 0.15$, 0.25, and 0.62 and (b) $\Theta = 0.25$ and different values of $\hat{d} = 0.001$, 0.005, and 0.023. The curves of β_c vs Θ and β_c vs $\hat{d}$ are shown in the insets.

Figure 2(b) shows the MS curves for a given Shields number Θ and different values of relative roughness $\hat{d}$. As the Shields number is kept constant in Fig. 2(b), it suggests that the particle size remains a constant. Therefore, an increase in relative roughness suggests a decrease in flow depth. At O(ε), the unstable region appears to diminish strikingly, as the relative roughness increases [Fig. 2(b)]. This is owing to a change in the friction factor, in accord with Eq. (7). The stabilizing effect remains effective for both shorter and longer wavenumbers. It indicates that even for the same aspect ratio, a small relative roughness is favorable for the formation of alternate bars with both shorter and longer wavenumbers, while a large relative roughness may favor their formation at intermediate wavenumbers. However, at O($\varepsilon\delta$) [see dashed lines in Fig. 2(b)], dissimilar results are found. Unlike the behavior of the MS curves at O(ε), for a given triplet (R_*, Θ, $\hat{d}$), the unstable region bounded by the MS curve at O($\varepsilon\delta$) appears to enhance with an increase in relative roughness. Note that the MS curves at O($\varepsilon\delta$) nearly overlap with those at O(ε) for shorter wavenumbers. In Fig. 2(b), the maximum value of relative roughness is set as 0.023, beyond which the MS curve at O($\varepsilon\delta$) yields an unrealistic

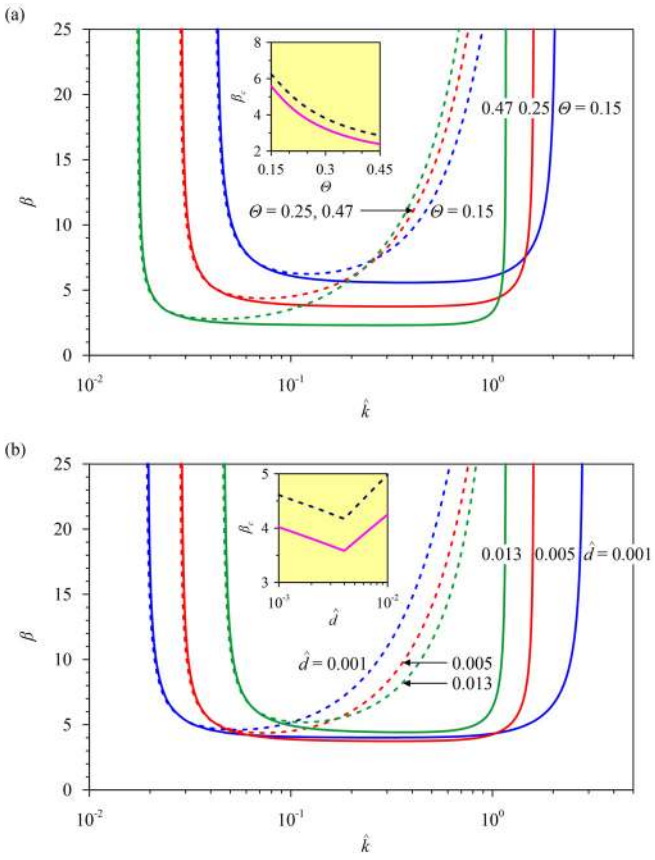

FIG. 3. The MS curves at the extremity of a smooth flow regime, $R_* = 3$ [solid lines: O(ε) and dashed lines: O($\varepsilon\delta$)]: (a) $\hat{d} = 0.005$ and different values of $\Theta = 0.15$, 0.25, and 0.47 and (b) $\Theta = 0.25$ and different values of $\hat{d} = 0.001$, 0.005, and 0.013. The curves of β_c vs Θ and β_c vs $\hat{d}$ are shown in the insets.

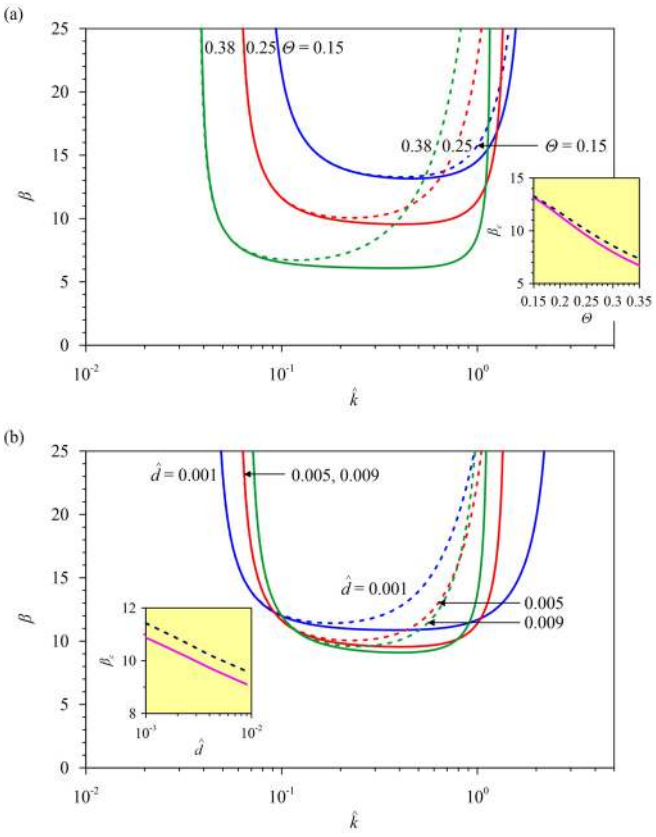

FIG. 4. The MS curves in a transitional flow regime, $R_* = 12$ [solid lines: O(ε) and dashed lines: O($\varepsilon\delta$)]: (a) $\hat{d} = 0.005$ and different values of $\Theta = 0.15$, 0.25, and 0.38 and (b) $\Theta = 0.25$ and different values of $\hat{d} = 0.001$, 0.005, and 0.009. The curves of β_c vs Θ and β_c vs $\hat{d}$ are shown in the insets.

region of instability. Therefore, $\hat{d}_m = 0.023$ is the limiting relative roughness of the bar formation in a smooth flow regime.

Akin to Fig. 2(a), the variations of threshold aspect ratio β_c with relative roughness $\hat{d}$ at both orders [O(ε) and O($\varepsilon\delta$)] are shown in the inset of Fig. 2(b). The behavior of $\beta_c(\hat{d})$ curves at O(ε) and O($\varepsilon\delta$) is similar. For a given order, the threshold aspect ratio reduces almost linearly with an increase in relative roughness reaching a minimum value and then, it increases in a linear fashion with a further increase in relative roughness. For a given relative roughness, the threshold aspect ratio at O($\varepsilon\delta$) appears to be larger than that O(ε). Note that the minima of $\beta_c(\hat{d})$ curves appear at $\hat{d} \approx 0.004$.

Figure 3 displays the MS curves at O(ε) and O($\varepsilon\delta$) at the extremity of a smooth flow regime ($R_* = 3$). In Fig. 3(a), the MS curves are shown for a given relative roughness $\hat{d}$ and different Shields numbers Θ, while in Fig. 3(b), they are shown for a given Shields number Θ and different values of relative roughness $\hat{d}$. Although the qualitative patterns of MS curves remain similar (see Figs. 2 and 3), it appears that for a given relative roughness at O(ε), the unstable region bounded by an MS curve changes considerably for intermediate wavenumbers as the Shields number increases [Fig. 3(a)]. The limiting values of Shields number and relative roughness are found to be $\Theta_m = 0.47$ and $\hat{d}_m = 0.013$. Unlike Fig. 2(a), the $\beta_c(\Theta)$ curves at O(ε) and O($\varepsilon\delta$) show that the threshold aspect ratio decreases with an increase in Shields number [see the inset of Fig. 3(a)]. On the other hand, the qualitative trends of $\beta_c(\hat{d})$ curves at O(ε) and O($\varepsilon\delta$) remain quite similar [see the insets of Figs. 2(b) and 3(b)].

Figure 4 presents the MS curves at O(ε) and O($\varepsilon\delta$) in a transitional flow regime ($R_* = 12$). In Fig. 4(a), the MS curves are shown for a given relative roughness $\hat{d}$ and different Shields numbers Θ, whereas in Fig. 4(b), those are shown for a given Shields number Θ and different values of relative roughness $\hat{d}$. It appears that the MS curves change strikingly, as the shear Reynolds number increases (compare Figs. 2 and 4). Unlike the MS curves at O(ε) in a smooth flow regime [see Fig. 2(a)], Fig. 4(a) displays that the unstable region confined to an MS curve increases with an increase in Shields number. Therefore, in a transitional flow regime ($R_* = 12$), the sediment suspension introduces a destabilizing effect, which appears to be pronounced for shorter wavenumbers. Thus, for the same aspect ratio, a large Shields number (small particle size) is favorable for the bar formation at shorter wavenumbers. The MS curves at O($\varepsilon\delta$) also show that that the unstable region bounded by an MS curve increases toward shorter wavenumbers, as the Shields number increases. Similar to a smooth

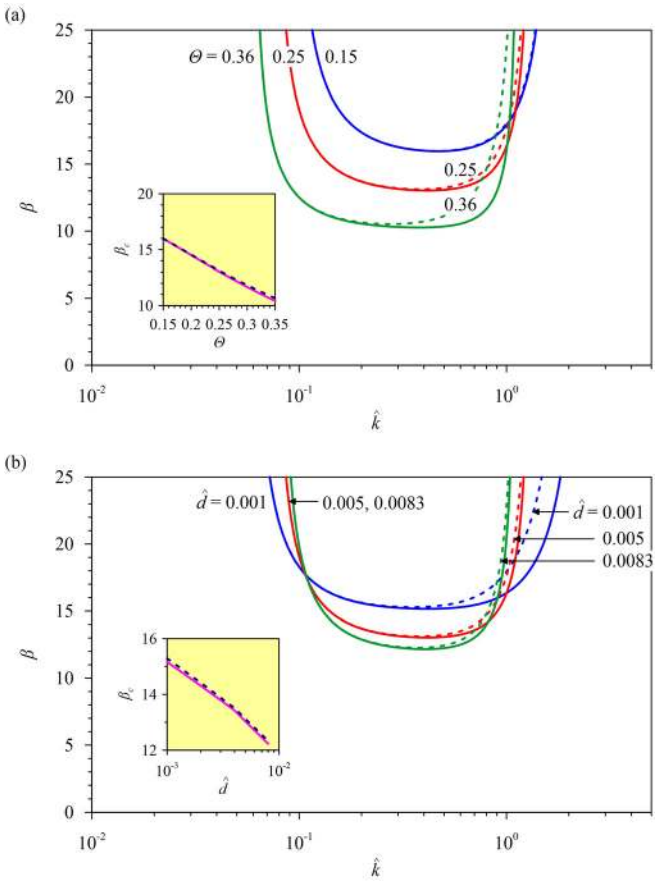

FIG. 5. The MS curves in a transitional flow regime, $R_* = 30$ [solid lines: O(ε) and dashed lines: O($\varepsilon\delta$)]: (a) $\hat{d} = 0.005$ and different values of $\Theta = 0.15$, 0.25, and 0.36 and (b) $\Theta = 0.25$ and different values of $\hat{d} = 0.001$, 0.005, and 0.0083. The curves of β_c vs Θ and β_c vs $\hat{d}$ are shown in the insets.

flow regime, for a given triplet (R_*, Θ, $\hat{d}$), the MS curve at O($\varepsilon\delta$) embraces smaller unstable region than that at O(ε). As expected, the MS curves at both O(ε) and O($\varepsilon\delta$) match for shorter wavenumbers. It is worth noting that for a given Shields number, the unstable region reduces significantly, as the shear Reynolds number increases [compare Figs. 2(a) and 4(a)]. In Fig. 4(a), the limiting Shields number of the formation of bars in a transitional flow regime ($R_* = 12$) corresponds to $\Theta_m = 0.38$. The $\beta_c(\Theta)$ curves at both orders [O(ε) and O($\varepsilon\delta$)] show that for a given order, the threshold aspect ratio reduces with an increase in Shields number [inset of Fig. 4(a)]. Note that for a given Shields number, the threshold aspect ratios at both orders are nearly equal. Further, it appears that for a given Shields number, the threshold aspect ratio at a given order in a transitional flow regime is larger than that in a smooth flow regime [compare Figs. 2(a) and 4(a)].

Figure 4(b) also shows that at O(ε), as the relative roughness increases, the unstable region reduces for shorter and longer wavenumbers, while that increases for intermediate wavenumbers. Similar to the features of the MS curves at O($\varepsilon\delta$) in a smooth flow regime [Fig. 2(b)], the unstable region at O($\varepsilon\delta$) in a transitional flow regime increases, as the relative roughness increases [Fig. 4(b)]. For a given triplet (R_*, Θ, $\hat{d}$), the MS curve at O($\varepsilon\delta$) produces smaller unstable region than that at O(ε). The MS curves at O(ε) perfectly coincide with those at O($\varepsilon\delta$) for shorter wavenumbers. It also appears that for a given relative roughness, the unstable region decreases substantially, as the shear Reynolds number increases [compare Figs. 2(b) and 4(b)]. In Fig. 4(b), $\hat{d}_m = 0.009$ represents the limiting relative roughness of the formation of bars in a transitional flow regime ($R_* = 12$). In the inset of Fig. 4(b), the $\beta_c(\Theta)$ curves at both orders [O(ε) and O($\varepsilon\delta$)] display a near-linear decreasing trend of the threshold aspect ratio with relative roughness. Note that for a given relative roughness, the threshold aspect ratio at a given order increases with an increase in shear Reynolds number [compare Figs. 2(b) and 4(b)].

As the transitional flow regime spans over a wide range of shear Reynolds numbers ($3 < R_* < 70$), it is interesting to explore the behavior of the MS curves with a further increase in shear Reynolds number in this flow regime. Figure 5 shows the MS curves at O(ε) and O($\varepsilon\delta$) in a transitional flow regime for $R_* = 30$. The MS curves for a given relative roughness $\hat{d}$ and different Shields numbers Θ are shown in Fig. 5(a), while those for a given Shields number Θ and different values of relative roughness $\hat{d}$ are shown in Fig. 5(b). It is noticeable that for a given triplet (R_*, Θ, $\hat{d}$), the unstable region for a given order reduces with an increase in shear Reynolds number (compare Figs. 4 and 5). The trends of the MS curves at O(ε) and O($\varepsilon\delta$) for $R_* = 30$ remain similar to those for $R_* = 12$. Unlike Fig. 4(a), it appears that for a small Shields number (say, $\Theta = 0.15$), the MS curves at both O(ε) and O($\varepsilon\delta$) coincide, as the shear Reynolds number increases [Fig. 5(a)]. However, for $\Theta > 0.15$, the MS curve at O($\varepsilon\delta$) holds slightly smaller unstable region than that at O(ε). As the shear Reynolds number increases, the MS curves at both O(ε) and O($\varepsilon\delta$) match for shorter and intermediate wavenumbers [Fig. 5(a)]. The limiting Shields number is found to reduce from $\Theta_m = 0.38$ to $\Theta_m = 0.36$, as the shear Reynolds number increases from $R_* = 12$ to 30. The $\beta_c(\Theta)$ curves [see the inset of Fig. 5(a)] indicate that for a given Shields number, the threshold aspect ratios at both orders remain the same. For a given Shields number, the threshold aspect ratio at a given order for $R_* = 30$ is larger than that for $R_* = 12$ [compare insets of Figs. 4(a) and 5(a)]. Unlike Fig. 4(b), as the shear Reynolds number increases, the MS curve at O($\varepsilon\delta$), for a small relative roughness ($\hat{d} = 0.001$), occupies an unstable region being of the order of the unstable region formed by the MS curve at O(ε) [Fig. 5(b)]. For $\hat{d} > 0.001$, the MS curves at O(ε) almost coincide with those at O($\varepsilon\delta$), as the shear Reynolds number increases [compare Figs. 4(b) and 5(b)]. Therefore, for $\hat{d} > 0.001$, the unstable regions created by the MS curves at O(ε) and O($\varepsilon\delta$) become nearly equal for $R_* = 30$. Comparison of Figs. 4(b) and 5(b) reveals that the limiting relative roughness reduces from $\hat{d}_m = 0.009$ to 0.0083 with an increase in shear Reynolds number from $R_* = 12$ to 30. The inset of Fig. 5(b) shows that for a given relative roughness, the threshold aspect ratios at both orders are almost equal. Comparison of the insets of Figs. 4(b) and 5(b) suggests that for a given relative roughness, the threshold aspect ratio at a given order for $R_* = 30$ is larger than that for $R_* = 12$.

Figure 6 displays the MS curves at O(ε) and O($\varepsilon\delta$) in a rough flow regime ($R_* = 100$). In Fig. 6(a), the MS curves are shown for a given relative roughness $\hat{d}$ and different Shields numbers Θ, whereas in Fig. 6(b), those are shown for a given Shields number Θ and

different values of relative roughness $\hat{d}$. The MS curves contract strikingly with an increase in shear Reynolds number, producing smaller unstable region (compare Figs. 5 and 6). Similar to a transitional flow regime, the MS curves at O(ε) in a rough flow regime shows that the unstable region bounded by an MS curve increases with an increase in Shields number, destabilizing shorter wavenumbers owing to the presence of sediment suspension. At O($\varepsilon\delta$), as the Shields number increases, the MS curves reveal that that the unstable region increases toward shorter wavenumbers. Unlike smooth and transitional flow regimes, the MS curve at O($\varepsilon\delta$) in a rough flow regime embraces the same unstable region as that at O(ε) [Fig. 6(a)], as the MS curves at both orders coincide. The limiting Shields number in Fig. 6(a) corresponds to $\Theta_m = 0.34$. Similar to a transitional flow regime, the $\beta_c(\Theta)$ curves in the inset of Fig. 6(a) at both orders [O(ε) and O($\varepsilon\delta$)] overlap perfectly. However, for a given Shields number, the threshold aspect ratio at a given order in a rough flow regime appears to be larger than those in smooth and transitional flow regimes. Akin to a transitional flow regime, the MS curves at O(ε) for different values of relative roughness in a rough flow regime show that the unstable region, for a given relative roughness, increases toward smaller aspect ratios with intermediate wavenumbers, as the relative roughness increases [Fig. 6(b)]. The MS curves at O(ε) and O($\varepsilon\delta$) in a rough flow regime, for a given relative roughness, produce an identical unstable region. The limiting relative roughness in Fig. 6(b) is found to be $\hat{d}_m = 0.007\,8$. In the inset of Fig. 6(b), the $\beta_c(\Theta)$ curves at both orders [O(ε) and O($\varepsilon\delta$)] almost overlap. Note that for a given relative roughness, the threshold aspect ratio at a given order in a rough flow regime is larger than those in smooth and transitional flow regimes.

Figs. 2–6 do not show how an MS curve, for a given relative roughness and Shields number, evolves with the shear Reynolds number. It is therefore interesting to explore the sensitivity of an MS curve to various flow regimes. To this end, Fig. 7 presents the MS curves for different shear Reynolds numbers ($R_* = 1$, 3, 12, 30, and 100) belonging to hydraulically smooth, extremity of smooth, transitional, and rough flow regimes. The relative roughness and the Shields number are considered as $\hat{d} = 0.005$ and $\Theta = 0.25$, respectively. The unstable region appears to contract with an increase in shear Reynolds number. At O(ε), the MS curves stabilize shorter and longer wavenumbers, as the shear Reynolds number increases. By contrast, at O($\varepsilon\delta$), the MS curves destabilize longer wavenumbers, as the shear Reynolds number increases. In smooth ($R_* = 1$), extremity of smooth ($R_* = 3$), and transitional ($R_* = 12$ and 30) flow regimes, the unstable region bounded by the MS curve at O(ε) appears to be larger than that at O($\varepsilon\delta$). However, in a rough flow regime ($R_* = 100$), the MS curves at both orders become identical. In essence, Fig. 7 offers an understanding of how the MS curves evolve with the shear Reynolds number. In addition, it provides a qualitative prediction of the MS curves for an intermediate shear Reynolds number between any two neighboring shear Reynolds numbers, as shown in Fig. 7. The inset of Fig. 7 shows the $\beta_c(R_*)$ curves at both orders [O(ε) and O($\varepsilon\delta$)]. The threshold aspect ratio for a given order increases with an increase in shear Reynolds number. Note that for a given order, a point of inflection is noticeable in the $\beta_c(R_*)$ curve. For the chosen values of relative roughness and Shields number, the threshold aspect ratio, for a given shear Reynolds number, at O($\varepsilon\delta$) appears to be slightly larger than that at O(ε) up to $R_* = 20$. However, in a rough flow regime, both the orders predict the same threshold aspect ratio.

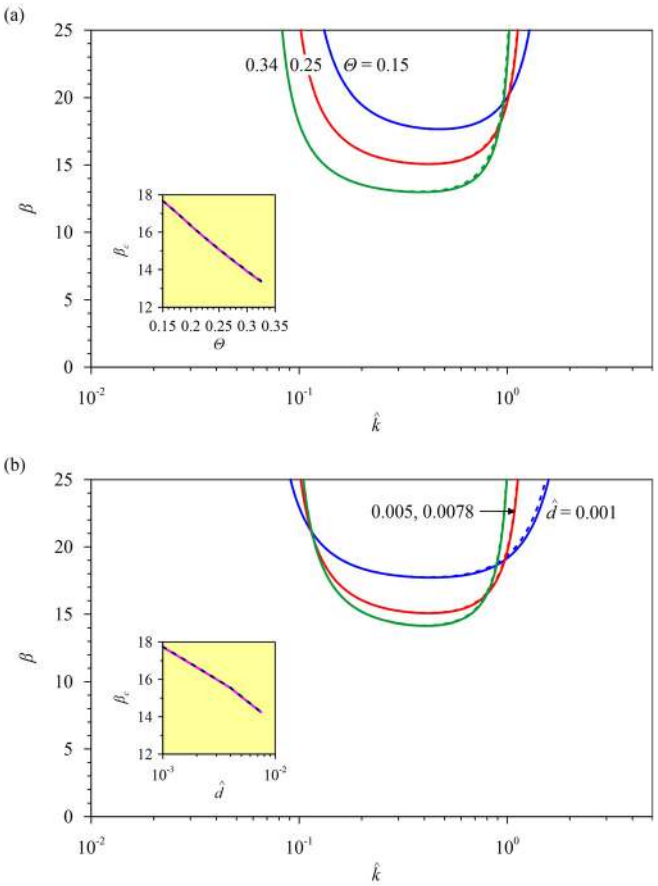

FIG. 6. The MS curves in a rough flow regime, $R_* = 100$ [solid lines: O(ε) and dashed lines: O($\varepsilon\delta$)]: (a) $\hat{d} = 0.005$ and different values of $\Theta = 0.15$, 0.25, and 0.34 and (b) $\Theta = 0.25$ and different values of $\hat{d} = 0.001$, 0.005, and 0.007 8. The curves of β_c vs Θ and β_c vs $\hat{d}$ are shown in the insets.

As discussed previously, the maximum values of Shields number and relative roughness for a given flow regime in Figs. 2–6 indicate their limiting values Θ_m and $\hat{d}_m$, respectively. The limiting values correspond to a critical flow, for which the flow Froude number is unity. Beyond the limiting values of Θ_m and $\hat{d}_m$, the theoretical results at O($\varepsilon\delta$) produce two unstable regions. Among them, the first unstable region favors the formation of bars beyond a threshold aspect ratio, as furnished in Figs. 2–6. The second unstable region (not shown here) suggests the formation of bars at all aspect ratios, thus contradicting the first unstable region in addition to a large corpus of theoretical and experimental observations. Therefore, the second unstable region appearing at longer wavenumbers represents an infeasible solution on the $\beta(\hat{k})$ plane.

It is further interesting to explore the variations of limiting values of Shields number and relative roughness, Θ_m and $\hat{d}_m$, respectively, with shear Reynolds number R_*. Figure 8 shows the curves of $\Theta_m(R_*)$ (solid lines) and $\hat{d}_m(R_*)$ (dashed lines) for different values of relative roughness and Shields number, respectively. The $\Theta_m(R_*)$ curves indicate that for a given relative roughness, the limiting Shields number reduces with an increase in shear Reynolds number. In addition, for a

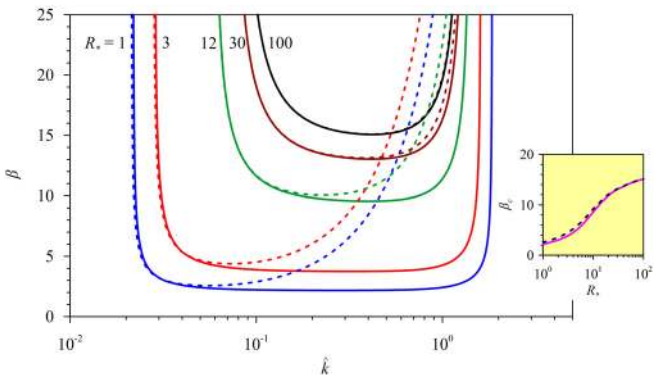

FIG. 7. Sensitivity of the MS curves to flow regimes for different values of $R_* = 1$, 3, 12, 30, and 100 [solid lines: O(ε) and dashed lines: O($\varepsilon\delta$)]. The $\hat{d} = 0.005$ and $\Theta = 0.25$ are considered. The β_c vs R_* is shown in the insets.

given shear Reynolds number, the limiting Shields number reduces, as the relative roughness increases. The $\hat{d}_m(R_*)$ curves show that for a given Shields number, the limiting relative roughness reduces with an increase in shear Reynolds number. On the other hand, for a given shear Reynolds number, the limiting relative roughness reduces, as the Shields number increases. In general, Fig. 8 displays that the variations of $\Theta_m(R_*)$ and $\hat{d}_m(R_*)$ are more prominent in a smooth flow regime as compared to those in transitional and rough flow regimes.

It is pertinent to mention that the major focus of this study is to explore the stability of free river bars from a linear stability perspective in weakly varying turbulent flows carrying significant load of sediment suspension. The key finding of this study is that the behavior of stability curves at the leading and next orders of approximation largely depends on the values of shear Reynolds number, Shields number, and relative roughness. Another important outcome of this study, being unidentified in the previous studies, is that the analysis limits the values of Shields number and relative roughness, beyond which results at the next order show that the alternate bars are unable to develop. However, this study does not take into account the effects of flow

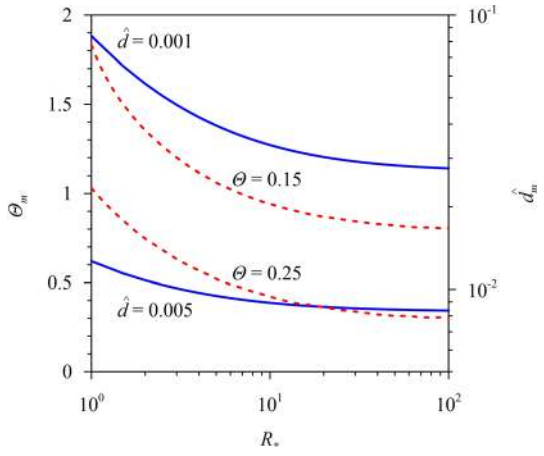

FIG. 8. Limiting Shields number Θ_m vs R_* for $\hat{d} = 0.001$ and 0.005 (solid lines) and limiting relative roughness $\hat{d}_m$ vs R_* for $\Theta = 0.15$ and 0.25 (dashed lines).

unsteadiness.[6,10] In this regard, Hall[10] reported linear and weakly nonlinear stability analyses of alternate bars that develop in an unsteady flow. However, the effects of sediment suspension were overlooked in Hall's[10] mathematical formulation. Therefore, a direct comparison of this study with the linear results of Hall[10] is not feasible. Note that some preliminary conclusions of this study are in agreement with the previous work of Federici and Seminara,[11] as discussed before. It is however important to highlight that the key results of this study may offer guidelines for new research pathways, including the sensitivity of free bars to the combined effects of flow unsteadiness, flow regimes, and bedload and suspended load transport.

V. CONCLUSIONS

A linear stability analysis of free river bars in weakly varying flows with dominant sediment suspension is presented. The analysis is done at leading and next orders of approximation. The behavior of stability curves is explored in different flow regimes. The results of linear stability analysis are discussed for different values of Shields number and relative roughness.

In a smooth flow regime, the threshold aspect ratio for a given order increases with an increase in Shields number reaching a peak value and thereafter reduces with a further increase in Shields number. By contrast, the threshold aspect ratio reduces with an increase in relative roughness attaining a minimum value and then, it increases monotonically, as the relative roughness increases further. On the other hand, in transitional and rough flow regimes, the threshold aspect ratio for a given order reduces, as the Shields number and relative roughness increase. For a given shear Reynolds number, the Shields number and the relative roughness play a decisive role in governing the bar instability. The former reflects the role of significant sediment suspension, while the latter takes into account the effects of frictional resistance.

At the leading order, as the shear Reynolds number increases, shorter and longer wavenumbers are stabilized. However, at the next order, the marginal stability curves destabilize longer wavenumbers with an increase in shear Reynolds number. The unstable region for a given order contracts significantly with an increase in shear Reynolds number. In smooth and transitional flow regimes, the unstable region at the leading order is larger than that at the next order. By contrast, in a rough flow regime, the leading and next orders produce the same region of instability.

In essence, this study offers an insight into the instability of free bars in weakly varying flows, highlighting the role of shear Reynolds number at different orders of approximation. The analysis is capable to address the effects of Shields number and relative roughness on the stability curves in different flow regimes. However, the analysis is primarily focused on the free bar instability from a linear perspective. Therefore, predicting the bar amplitude in an unsteady flow covering different flow regimes by using a nonlinear approach remains an interesting aspect as a future scope of research. In addition, analytical predictions of bar wavelength and bar amplitude in gravel-bed rivers remain a challenging task. This arises owing to the complex fluid-sediment interaction in the near-bed flow layer[44–47] together with the sediment transport.[48,49] To resolve this issue, researchers need to use a 3D framework in modeling the near-bed flow, turbulent characteristics, and sediment transport.

ACKNOWLEDGMENTS

S.D. acknowledges the J C Bose Fellowship Award [Funded by DST | Science and Engineering Research Board (SERB), Grant No. JCB/2018/000004] in pursuing this work.

APPENDIX A: ESTIMATION OF Θ_S

According to van Rijn,[28] the condition required for the initiation of sediment suspension is the saltating length of a particle exceeding 100 times the particle size. He proposed following empirical relationships:

$$\frac{u_{*s}}{W_s}(1 < D_* \leq 10) = \frac{4}{D_*}, \tag{A1}$$

$$\frac{u_{*s}}{W_s}(D_* > 10) = 0.4. \tag{A2}$$

In the above, u_{*s} is the shear velocity at the threshold of sediment suspension. With u_{*s}, the Shields number Θ_s at the threshold of sediment suspension can be obtained from Eq. (9). For the estimation of settling velocity W_s, Wu and Wang[50] proposed an empirical formula as follows:

$$W_s = \frac{P}{Q}\cdot\frac{\upsilon}{d}\left\{\left[\frac{1}{4} + \left(\frac{4Q}{3P}D_*^3\right)^{1/q}\right]^{0.5} - \frac{1}{2}\right\}, \tag{A3}$$

where P and Q are the coefficients and q is an exponent. They are expressed as $P = 53.5\exp(-0.65S_p)$, $Q = 5.65\exp(-2.5S_p)$, and $q = 0.7 + 0.9S_p$, where S_p is the Corey shape factor (≈ 0.7 for natural particles).

APPENDIX B: EXPRESSIONS FOR C_0, K_0, AND K_1

The depth-averaged concentration at the leading order C_0 in Eq. (20) is expressed as[11]

$$C_0 = \frac{1}{1-\hat{a}}C_a I_1, \tag{B1}$$

where $\hat{a} = a/D$, a is the reference level that acts as the interface separating the bedload and the suspended load particles, C_a is the reference concentration, and I_1 is the integral function. For a and C_a, several empirical formulas exist in the literature.[28,51,52] Here, we use van Rijn's[28] relationships as follows:

$$C_a = 0.015\frac{d}{a}\left(\frac{\Theta}{\Theta_c} - 1\right)D_*^{-0.3}, \tag{B2}$$

$$a(k_s < 0.01D) = 0.01D,\ a(k_s \geq 0.01D) = k_s. \tag{B3}$$

The integral function I_1 in Eq. (B1) is expressed as

$$I_1 = \int_{\hat{a}}^{1}\left(\frac{\hat{a}}{1-\hat{a}}\cdot\frac{1-\hat{z}}{\hat{z}}\right)^{\zeta}\mathrm{d}\hat{z}, \tag{B4}$$

where $\hat{z} = z/D$, z is the vertical distance from the channel bed, and ζ is the Rouse number that quantifies the settling velocity relative to the shear velocity. The ζ is expressed as

$$\zeta = \frac{W_s S_c}{\kappa u_*}, \tag{B5}$$

where S_c is the turbulent Schmidt number (≈ 1) and κ is the von Kármán coefficient ($= 0.41$).

The function K_0 in Eq. (20) is expressed as[11]

$$K_0 = \frac{C_f^{0.5}}{\kappa}(1-\hat{a})\left(\frac{I_2}{I_1} + K_2\right), \tag{B6}$$

where C_f is the conductance coefficient ($= f/8$), I_2 is the integral function, and K_2 is a function that depends on C_f. The I_2 and K_2 are expressed as

$$I_2 = \int_{\hat{a}}^{1}(\ln\hat{z} + 1.84\hat{z}^2 - 1.56\hat{z}^3)\left(\frac{\hat{a}}{1-\hat{a}}\cdot\frac{1-\hat{z}}{\hat{z}}\right)^{\zeta}\mathrm{d}\hat{z}, \tag{B7}$$

$$K_2 = 0.777 + \frac{\kappa}{C_f^{0.5}}. \tag{B8}$$

In addition, the function K_1 in Eq. (20) is expressed as[11]

$$K_1 = \frac{C_f^{0.5}}{\kappa}K_3, \tag{B9}$$

where K_3 is a function of $\hat{a}$ and ζ. The K_3 has the following form:[43]

$$K_3 = \int_{\hat{a}}^{1} C_{12}(\ln\hat{z} + 1.84\hat{z}^2 - 1.56\hat{z}^3)\mathrm{d}\hat{z} - \ln\hat{z}_0\int_{\hat{a}}^{1} C_{12}\mathrm{d}\hat{z}, \tag{B10}$$

where $\hat{z}_0 = z_0/D$, z_0 is the zero-velocity level where streamwise velocity (x component) vanishes according to the logarithmic law,[27] and C_{12} is a function. The C_{12} is obtained from the solution of the following differential equation:

$$\frac{\partial C_{12}}{\partial\hat{z}} + \frac{1}{\zeta}\left\{\frac{\partial}{\partial\hat{z}}\left[\hat{z}(1-\hat{z})\frac{\partial}{\partial\hat{z}}\right]\right\}C_{12} = \frac{(1-\hat{a})C_f^{0.5}}{\kappa I_1}\left(\ln\frac{\hat{z}}{\hat{z}_0} + 1.84\hat{z}^2 - 1.56\hat{z}^3\right)\left(\frac{\hat{a}}{1-\hat{a}}\cdot\frac{1-\hat{z}}{\hat{z}}\right)^{\zeta}. \tag{B11}$$

The boundary conditions associated with Eq. (B11) are expressed as

$$C_{12}(\hat{z} = 1) = 0, \tag{B12}$$

$$\frac{\partial C_{12}}{\partial\hat{z}}(\hat{z} = \hat{a}) = 0. \tag{B13}$$

Equation (B11) is solved numerically using a shooting technique.[53]

APPENDIX C: COEFFICIENTS s_j AND PERTURBATIONS ψ_{010}, ψ_{011}, AND ψ_{110}

The coefficients s_j ($j = 1$ to 4) in Eqs. (24) and (26) are expressed as

$$s_1 = 2\left(1 - \frac{\Theta_0}{f_0}\cdot\frac{\partial f}{\partial\Theta}\right)^{-1},\quad s_2 = \frac{1}{f_0}\cdot\frac{\partial f}{\partial\hat{D}}\left(1 - \frac{\Theta_0}{f_0}\cdot\frac{\partial f}{\partial\Theta}\right)^{-1},$$
$$s_3 = \frac{\Theta_0}{\Phi_0}\cdot\frac{\partial\Phi}{\partial\Theta}s_1,\quad s_4 = \frac{\Theta_0}{\Phi_0}\cdot\frac{\partial\Phi}{\partial\Theta}s_2 + \frac{1}{\Phi_0}\cdot\frac{\partial\Phi}{\partial\hat{D}}. \tag{C1}$$

We express the perturbations ψ_{010}, ψ_{011}, and ψ_{110} in terms of the perturbations of the primitive variables as

$$\psi_{010} = t_1 \hat{U}_{10} + t_2 \hat{D}_{10}, \tag{C2}$$

$$\psi_{011} = t_1 \hat{U}_{11} + t_2 \hat{D}_{11}, \tag{C3}$$

$$\psi_{110} = g_1 \frac{\partial \hat{U}_{10}}{\partial \hat{x}} + g_2 \frac{\partial \hat{D}_{10}}{\partial \hat{x}}. \tag{C4}$$

In the above, t_1, t_2, g_1, and g_2 are expressed as

$$t_1 = s_1 \left\{ \frac{\Theta_0}{2f_0} \cdot \frac{\partial f}{\partial \Theta} + \frac{1.5\Theta_0}{\Theta_0 - \Theta_c} - 0.5(I_{20} + K_{20} I_{10})^{-1} \times \left[\zeta_0 (I_{21} + K_{20} I_{11}) + \frac{\kappa \Theta_0 I_{10}}{f_0 C_{f0}^{0.5}} \cdot \frac{\partial f}{\partial \Theta} \right] \right\}, \tag{C5}$$

$$t_2 = s_2 \left\{ \frac{1}{2} - \frac{1}{s_2} + \frac{1.5\Theta_0}{\Theta_0 - \Theta_c} - 0.5(I_{20} + K_{20} I_{10})^{-1} \times \left[\zeta_0 (I_{21} + K_{20} I_{11}) + \frac{\kappa I_{10}}{C_{f0}^{0.5}} \right] \right\}, \tag{C6}$$

$$g_1 = \frac{s_1 C_{a0} K_{10}}{1 - \hat{a}} \left(\frac{1.5\Theta_0}{\Theta_0 - \Theta_c} I_{10} - 0.5\zeta_0 I_{11} \right), \tag{C7}$$

$$g_2 = \frac{s_2 C_{a0} K_{10}}{1 - \hat{a}} \left[\left(\frac{1.5\Theta_0}{\Theta_0 - \Theta_c} - \frac{1}{s_2} \right) I_{10} - 0.5\zeta_0 I_{11} \right], \tag{C8}$$

where ζ_0, C_{f0}, C_{a0}, I_{10}, I_{20}, and K_{20} are the values of Rouse number, conductance coefficient, reference concentration, I_1, I_2, and K_2 for the undisturbed flow, respectively. The I_{11} and I_{21} are expressed as

$$I_{11} = \int_{\hat{a}}^{1} \left(\frac{\hat{a}}{1 - \hat{a}} \cdot \frac{1 - \hat{z}}{\hat{z}} \right)^{\zeta_0} \ln \left(\frac{\hat{a}}{1 - \hat{a}} \cdot \frac{1 - \hat{z}}{\hat{z}} \right) \mathrm{d}\hat{z}, \tag{C9}$$

$$I_{21} = \int_{\hat{a}}^{1} (\ln \hat{z} + 1.84\hat{z}^2 - 1.56\hat{z}^3) \left(\frac{\hat{a}}{1 - \hat{a}} \cdot \frac{1 - \hat{z}}{\hat{z}} \right)^{\zeta_0} \ln \left(\frac{\hat{a}}{1 - \hat{a}} \cdot \frac{1 - \hat{z}}{\hat{z}} \right) \mathrm{d}\hat{z}. \tag{C10}$$

DATA AVAILABILITY

The data that support the findings of this study are available from the corresponding author upon reasonable request.

REFERENCES

[1] S. Dey and S. Z. Ali, "Fluvial instabilities," Phys. Fluids **32**(6), 061301 (2020).
[2] S. Lanzoni and M. Tubino, "Grain sorting and bar instability," J. Fluid Mech. **393**, 149–174 (1999).
[3] M. Redolfi, M. Welber, M. Carlin, M. Tubino, and W. Bertoldi, "Morphometric properties of alternate bars and water discharge: A laboratory investigation," Earth Surf. Dyn. **8**(3), 789–808 (2020).
[4] B. Federici and G. Seminara, "On the convective nature of bar instability," J. Fluid Mech. **487**, 125–145 (2003).
[5] M. Tubino, R. Repetto, and G. Zolezzi, "Free bars in rivers," J. Hydraul. Res. **37**(6), 759–775 (1999).
[6] M. Tubino, "Growth of alternate bars in unsteady flow," Water Resour. Res. **27**(1), 37–52, https://doi.org/10.1029/90WR01699 (1991).
[7] S. Z. Ali and S. Dey, "Interfacial instability of sand patterns induced by turbulent shear flow," Int. J. Sed. Res. (in press) (2021).
[8] S. Z. Ali and S. Dey, "Instability of large-scale riverbed patterns," Phys. Fluids **33**(1), 015109 (2021).
[9] M. Colombini, G. Seminara, and M. Tubino, "Finite-amplitude alternate bars," J. Fluid Mech. **181**, 213–232 (1987).
[10] P. Hall, "Alternating bar instabilities in unsteady channel flows over erodible beds," J. Fluid Mech. **499**, 49–73 (2004).
[11] B. Federici and G. Seminara, "Effect of suspended load on sandbar instability," Water Resour. Res. **42**(7), W07407, https://doi.org/10.1029/2005WR004399 (2006).
[12] M. B. Bertagni and C. Camporeale, "Finite amplitude of free alternate bars with suspended load," Water Resour. Res. **54**(12), 9759–9773, https://doi.org/10.1029/2018WR022819 (2018).
[13] R. Kinoshita, "Investigation of channel deformation in Ishikari River," Report of the Bureau of Resources, Department of Science and Technology, Tokyo, Japan, 1961.
[14] Y. Fujita, "Fundamental study on channel changes in alluvial rivers," D.Eng. thesis (Kyoto University, Kyoto, Japan, 1980).
[15] M. Iguchi, "Tests for fine gravel transport in a large laboratory flume," Report of the National Science Foundation, School of Earth Science, Tsukuba University, Ibaragi, Japan, 1980.
[16] S. Ikeda, "Prediction of alternate bar wavelength and height," J. Hydraul. Eng. **110**(4), 371–386 (1984).
[17] A. Crosato, F. B. Desta, J. Cornelisse, F. Schuurman, and W. S. J. Uijttewaal, "Experimental and numerical findings on the long-term evolution of migrating alternate bars in alluvial channels," Water Resour. Res. **48**(6), W06524, https://doi.org/10.1029/2011WR011320 (2012).
[18] J. P. C. Eekhout, A. J. F. Hoitink, and E. Mosselman, "Field experiment on alternate bar development in a straight sand-bed stream," Water Resour. Res. **49**(12), 8357–8369, https://doi.org/10.1002/2013WR014259 (2013).
[19] M. T. Ramirez and M. A. Allison, "Suspension of bed material over sand bars in the Lower Mississippi River and its implications for Mississippi delta environmental restoration," J. Geophys. Res.: Earth Surf. **118**(2), 1085–1104, https://doi.org/10.1002/jgrf.20075 (2013).
[20] A. Defina, "Numerical experiments on bar growth," Water Resour. Res. **39**(4), 1092, https://doi.org/10.1029/2002WR001455 (2003).
[21] A. Siviglia, G. Stecca, D. Vanzo, G. Zolezzi, E. F. Toro, and M. Tubino, "Numerical modelling of two-dimensional morphodynamics with applications to river bars and bifurcations," Adv. Water Resour. **52**, 243–260 (2013).
[22] A. Crosato and E. Mosselman, "An integrated review of river bars for engineering, management and transdisciplinary research," Water **12**(2), 596 (2020).
[23] B. de Saint-Venant, "Theorie du mouvement non permanent des eaux, avec application aux crues de rivieras et a l'introduction des marces dans leur lit," C. R. Acad. Sci. **73**, 147–154 (1871).
[24] F. M. Exner, "Über die wechselwirkung zwischen wasser und geschiebe inin flüssen," Sitzungsber Akad. Wiss. **134**, 165–203 (1925).
[25] C. F. Colebrook and C. M. White, "Experiments with fluid friction in roughened pipes," Proc. R. Soc. A **161**, 367–381 (1937).
[26] F. Engelund and E. Hansen, *A Monograph on Sediment Transport in Alluvial Streams* (Danish Technical Press, Copenhagen, 1967).
[27] S. Dey, *Fluvial Hydrodynamics: Hydrodynamic and Sediment Transport Phenomena* (Springer-Verlag, Berlin, Germany, 2014).
[28] L. C. van Rijn, "Sediment transport, Part II: Suspended load transport," J. Hydraul. Eng. **110**(11), 1613–1641 (1984).
[29] H. A. Einstein, "The bed-load function for sediment transportation in open channel flows," in *Technical Bulletin* (United States Department of Agriculture, Soil Conservation Service, Washington DC, USA, 1950), p. 1026.
[30] S. Ikeda, "Lateral bed load transport on side slopes," J. Hydraul. Div. **108**(11), 1369–1373 (1982).
[31] G. Parker, "Discussion on lateral bed load transport on side slopes," J. Hydraul. Eng. **110**(2), 197–199 (1984).
[32] S. Z. Ali and S. Dey, "Hydrodynamic instability of meandering channels," Phys. Fluids **29**(12), 125107 (2017).
[33] A. W. Baar, J. de Smit, W. S. J. Uijttewaal, and M. G. Kleinhans, "Sediment transport of fine sand to fine gravel on transverse bed slopes in rotating annular flume experiments," Water Resour. Res. **54**(1), 19–45, https://doi.org/10.1002/2017WR020604 (2018).
[34] A. M. Talmon, N. Struiksma, and M. C. L. M. Van Mierlo, "Laboratory measurements of the direction of sediment transport on transverse alluvial-bed slopes," J. Hydraul. Res. **33**(4), 495–517 (1995).

[35]E. Meyer-Peter and R. Müller, "Formulas for bed-load transport," in Proceedings of the 2nd Meeting of International Association for Hydraulic Research, Stockholm, Sweden (1948), Vol. 3, pp. 39–64.
[36]S. Z. Ali and S. Dey, "Origin of the scaling laws of sediment transport," Proc. R. Soc. A **473**, 20160785 (2017).
[37]S. Z. Ali and S. Dey, "Hydrodynamics of sediment threshold," Phys. Fluids **28**(7), 075103 (2016).
[38]S. Dey and S. Z. Ali, "Stochastic mechanics of loose boundary particle transport in turbulent flow," Phys. Fluids **29**(5), 055103 (2017).
[39]S. Dey and S. Z. Ali, "Mechanics of sediment transport: Particle scale of entrainment to continuum scale of bedload flux," J. Eng. Mech. **143**(11), 04017127 (2017).
[40]S. Dey and S. Z. Ali, "Review article: Advances in modeling of bed particle entrainment sheared by turbulent flow," Phys. Fluids **30**(6), 061301 (2018).
[41]S. Dey and S. Z. Ali, "Bed sediment entrainment by streamflow: State of the science," Sedimentology **66**(5), 1449–1485 (2019).
[42]W. Wu and S. S. Y. Wang, "Movable bed roughness in alluvial rivers," J. Hydraul. Eng. **125**(12), 1309–1312 (1999).
[43]M. Bolla Pittaluga and G. Seminara, "Depth-integrated modeling of suspended sediment transport," Water Resour. Res. **39**(5), 1137, https://doi.org/10.1029/2002WR001306 (2003).
[44]E. Padhi, N. Penna, S. Dey, and R. Gaudio, "Hydrodynamics of water-worked and screeded gravel beds: A comparative study," Phys. Fluids **30**(8), 085105 (2018).
[45]E. Padhi, N. Penna, S. Dey, and R. Gaudio, "Spatially averaged dissipation rate in flows over water-worked and screeded gravel beds," Phys. Fluids **30**(12), 125106 (2018).
[46]E. Padhi, N. Penna, S. Dey, and R. Gaudio, "Near-bed turbulence structures in water-worked and screeded gravel-bed flows," Phys. Fluids **31**(4), 045107 (2019).
[47]N. Penna, E. Padhi, S. Dey, and R. Gaudio, "Structure functions and invariants of the anisotropic Reynolds stress tensor in turbulent flows on water-worked gravel beds," Phys. Fluids **32**(5), 055106 (2020).
[48]R. Maurin, J. Chauchat, B. Chareyre, and P. Frey, "A minimal coupled fluid-discrete element model for bedload transport," Phys. Fluids **27**(11), 113302 (2015).
[49]D. Berzi and L. Fraccarollo, "Intense sediment transport: Collisional to turbulent suspension," Phys. Fluids **28**(2), 023302 (2016).
[50]W. Wu and S. S. Y. Wang, "Formulas for sediment porosity and settling velocity," J. Hydraul. Eng. **132**(8), 858–862 (2006).
[51]F. Engelund and J. Fredsøe, "A sediment transport model for straight alluvial channels," Hydrol. Res. **7**(5), 293–306 (1976).
[52]M. Garcia and G. Parker, "Entrainment of bed sediment into suspension," J. Hydraul. Eng. **117**(4), 414–435 (1991).
[53]R. S. Esfandiari, *Numerical Methods for Engineers and Scientists Using MATLAB®*, 2nd ed. (CRC Press, Boca Raton, 2017).